J. Fluid Mech. (2021), *vol*. 915, A100, doi:10.1017/jfm.2021.187

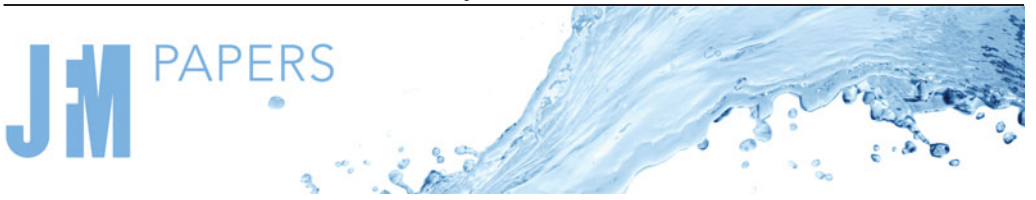

Shock detachment and drag in hypersonic flow over wedges and circular cylinders

H.G. Hornung†

Graduate Aerospace Laboratories, California Institute of Technology, Pasadena, CA 91125, USA

(Received 15 December 2020; revised 9 February 2021; accepted 23 February 2021)

In a recent publication, Hornung *et al.* (*J. Fluid Mech.*, vol. 871, 2019, pp. 1097–1116) showed that the shock wave stand-off distance and the drag coefficient of a cone in the inviscid hypersonic flow of a perfect gas can be expressed as the product of a function of the inverse normal-shock density ratio ε and a function of the cone-angle parameter η, thus reducing the number of independent parameters from three (Mach number, specific heat ratio and angle) to two. Analytical forms of the functions were obtained by performing a large number of Euler computations. In this article, the same approach is applied to a symmetrical flow over a wedge. It is shown that the same simplification applies and corresponding analytical forms of the functions are obtained. The functions of ε are compared with the newly determined corresponding functions for flow over a circular cylinder.

Key words: hypersonic flow, shock waves

1. Introduction

One of the most important parameters in hypersonic flow is the inverse normal-shock density ratio, which for a perfect gas is

$$\varepsilon = \frac{\rho_\infty}{\rho_s} = \frac{\gamma - 1 + 2/M_\infty^2}{\gamma + 1}, \tag{1.1}$$

where ρ is the density, γ is the ratio of specific heats and M is the Mach number. The subscripts ∞ and s refer to the free stream and to the immediate post-normal-shock condition, respectively.

In the flow over a wedge with given free-stream conditions, the shock wave is straight and attached to the wedge tip when the wedge half-angle θ is sufficiently small. As θ is increased, a point is reached at which the flow downstream of the shock is sonic so that information about the length of the wedge from tip to shoulder can be communicated to

† Email address for correspondence: hans@caltech.edu

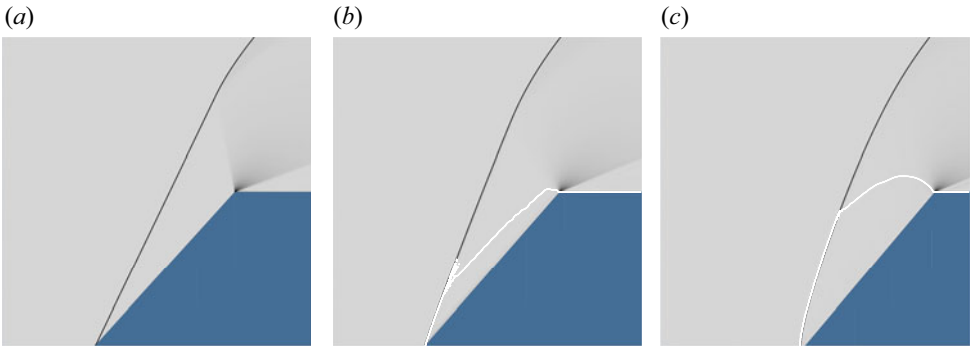

Figure 1. Results of computations of flow over a wedge at $M_\infty = 10$ and $\gamma = 1.3$ with $\theta = 48°$, 49° and 50°, showing (*a–c*) entirely supersonic flow with a straight attached shock, partly subsonic flow with a curved, attached shock and flow with a detached shock. The white line is the sonic line. The grey shading in these pseudo-schlieren images is proportional to a monotonic function of the density gradient.

the tip. The shock begins to curve and, at a slightly larger value of θ, detaches from the tip. The results of the Euler computations for these three conditions are shown in figure 1. An example of the importance of the parameter ε is the approximation given by Hayes & Probstein (1959) for the values of θ and the shock angle β at detachment:

$$\beta_d = \arctan\sqrt{\frac{1}{\varepsilon}}, \quad \theta_d = 2\beta_d - \frac{\pi}{2}. \tag{1.2a,b}$$

Here the subscript d refers to the detachment condition. The exact values of these detachment angles may be determined from

$$\beta_{de} = \arcsin\sqrt{\frac{(\gamma+1)M_\infty^2/4 - 1 + \sqrt{\gamma+1}\sqrt{(\gamma+1)M_\infty^4/16 + 1 + (\gamma-1)M_\infty^2/2}}{\gamma M_\infty^2}} \tag{1.3}$$

$$\theta_{de} = \arctan\left(\frac{(M_\infty^2 \sin^2\beta_{de} - 1)/\tan\beta_{de}}{1 + [(\gamma+1)/2 - \sin^2\beta_{de}]M_\infty^2}\right), \tag{1.4}$$

see e.g. Chapman (2000). Figure 2 shows the quality of the approximation of Hayes & Probstein (1959) by plotting exact values for Mach numbers between 4 and 10 and γ between 1.05 and 1.4 together with the approximation versus ε. As ε increases, the approximate value of θ_d is slightly above the exact curves, especially at the lower Mach numbers.

The range of θ for which the shock is detached is of particular interest here. As in Hornung, Schramm & Hannemann (2019), we introduce the variable

$$\eta = \frac{\theta - \theta_d}{\pi/2 - \theta_d}, \tag{1.5}$$

such that $\eta = 0$ at detachment and $\eta = 1$ at $\theta = \pi/2$. Because analytical formulae for the exact detachment angles exist in the case of a wedge flow, we use the variable

$$\eta_e = \frac{\theta - \theta_{de}}{\pi/2 - \theta_{de}} \tag{1.6}$$

in place of η.

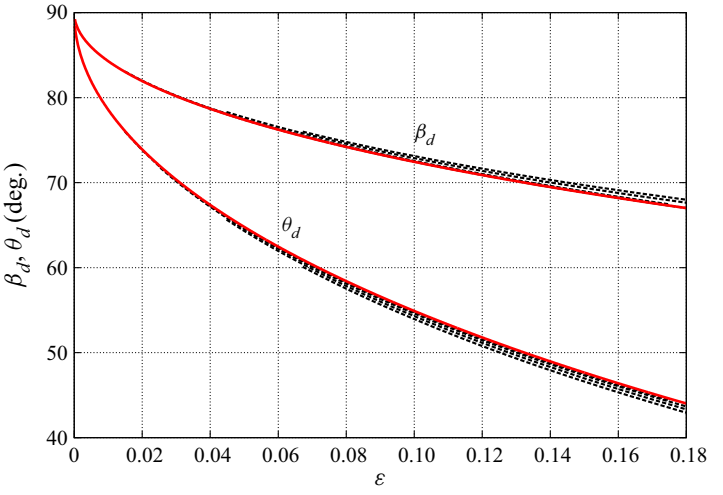

Figure 2. Exact detachment angles for $4 \leqslant M_\infty \leqslant 10$ and $1.05 \leqslant \gamma \leqslant 1.4$, plotted with black dashed lines, compared with the approximation of Hayes & Probstein (1959) (1.2*a*,*b*) in red.

For the shock stand-off distance, Δ, which is of special interest, we again make the hypothesis that it follows the functional form

$$\frac{\Delta}{H} = g(\varepsilon) f(\eta_e) \tag{1.7}$$

as in Hornung *et al.* (2019). Here H is the height of the wedge measured from the symmetry plane to the shoulder. To test the hypothesis, we perform a large number of computations covering the parameter space $(M_\infty, \gamma, \theta)$. If the hypothesis is true for the case of a flow over a wedge as it was for a cone flow, the results can be used to determine the functional forms of g and f.

2. Discussion of results of computations

2.1. *Shock stand-off distance*

The parameter space was explored by computing the flow over wedges using the Euler equations. Details about the computational technique are given in the Appendix. An example of the results is presented in figure 3 for the case of $M_\infty = 5$. Similar results were also obtained for $M_\infty = 4$, 7 and 10. Plotting the dimensionless shock stand-off distance against ε in the case of $\theta = 90^\circ$, (square slab), i.e. for $\eta_e = 1$, where $f(\eta_e) = f(1)$ is a constant, provides a partial test of the hypothesis for the function $g(\varepsilon)$.

This is shown in figure 4. A fit of the points in figure 4 yields the interesting result where all points fall on a unique curve given by

$$g(\varepsilon) = \sqrt{\varepsilon}\left(1 + \tfrac{3}{2}\varepsilon\right), \tag{2.1}$$

thus confirming the first part of the hypothesis, i.e. that a unique function $g(\varepsilon)$ exists. Again, as in the case of flow over cones, the leading term is proportional to $\sqrt{\varepsilon}$. An explanation for this, which applies equally to the plane case, has been given on the basis of a control volume argument in Hornung *et al.* (2019). The fact that all the results fall on the same curve confirms the first part of the hypothesis. It is interesting that in the corresponding function of ε for the 90° cone, the factor 3/2 that appears in (2.1) is 1/2.

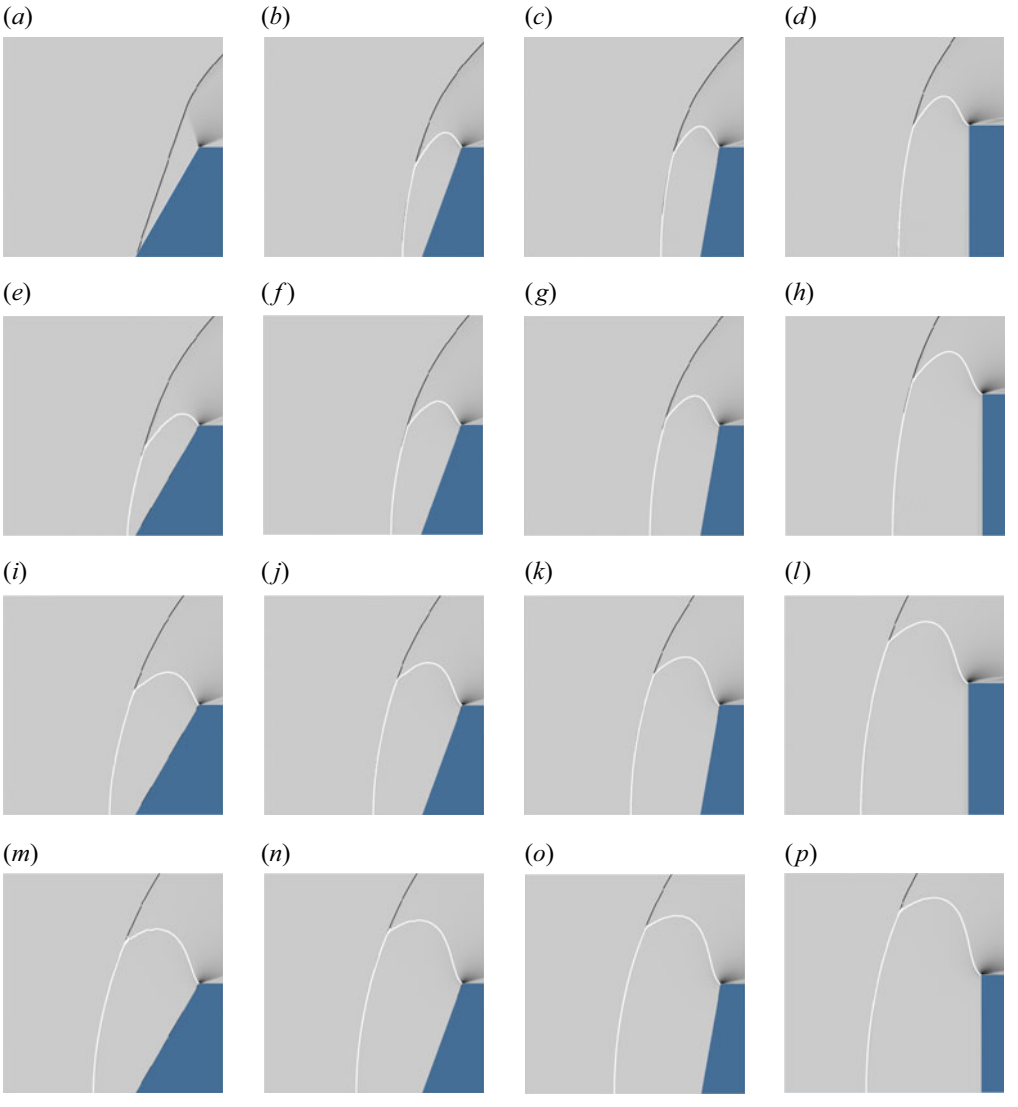

Figure 3. Pseudo-schlieren images of flow over a wedge at $M_\infty = 5$. The grey shading in these images is proportional to a monotonic function of the magnitude of the density gradient. The white line is the sonic line. In rows from left to right, $\theta = 60^\circ$, 70°, 80° and 90°. In columns from top to bottom, $\gamma = 1.05$, 1.1, 1.2 and 1.3. Similar sets of computations were made for $M_\infty = 4$, 7 and 10.

To test the second part of the hypothesis, four plots of $f(\eta_e) = \Delta/[Hg(\varepsilon)]$ versus η_e are shown in figure 5 for the four Mach numbers and the four γ values. All the computational results fall on the same curve given by the unique function

$$f(\eta_e) = 2.2\eta_e - 0.3\eta_e^2, \tag{2.2}$$

thus confirming the second part of the hypothesis. Note, however, the fit is not as good at $M_\infty = 4$ as that for the other values of M_∞. Had we used η instead of η_e, the deterioration of the fit at the lower Mach numbers would have been even larger.

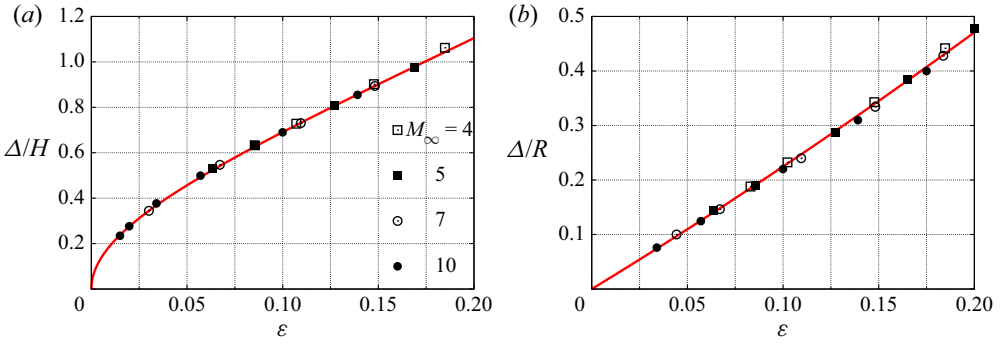

Figure 4. (*a*) Dimensionless shock stand-off distance for flow over a 90° wedge with $M_\infty = 4$, 5, 7 and 10 and $\gamma = 1.05$, 1.1, 1.2 and 1.3. In the case of $M_\infty = 10$, two cases of $\gamma = 1.01$ and 1.02, and with $M_\infty = 7$, one case with $\gamma = 1.02$ are added. (*b*) Corresponding plot for flow over a circular cylinder of radius R. In this case, the results are fitted well by $\Delta/R = 2.14\,\varepsilon(1 + \varepsilon/2)$. In Hornung (1972), the linear form $\Delta/R = 2.32\,\varepsilon$ was found, which is only slightly different.

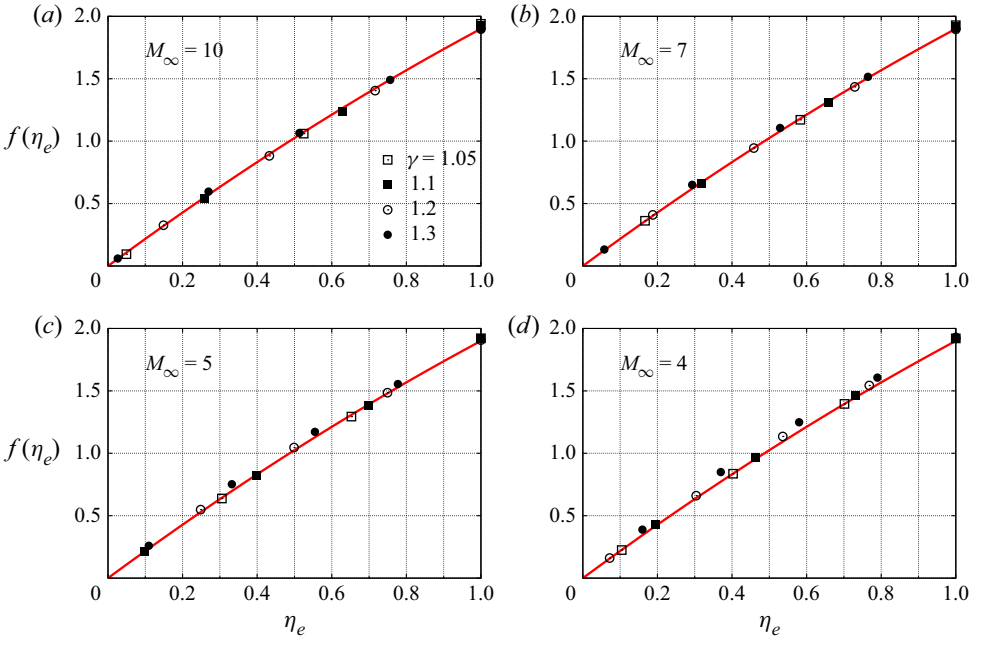

Figure 5. Four plots of $f(\eta_e)$ versus η_e. Top, left to right: $M_\infty = 10$ and 7. Bottom, left to right $M_\infty = 5$ and 4. In all four plots the curve is the same and given by (2.2).

2.2. *Drag coefficient*

Hornung *et al.* (2019) showed that for flow over cones, the drag coefficient could also be expressed in the form of (1.7). The drag coefficient for a wedge is written as

$$C_D = \frac{2D}{\gamma p_\infty M_\infty^2 HL}, \tag{2.3}$$

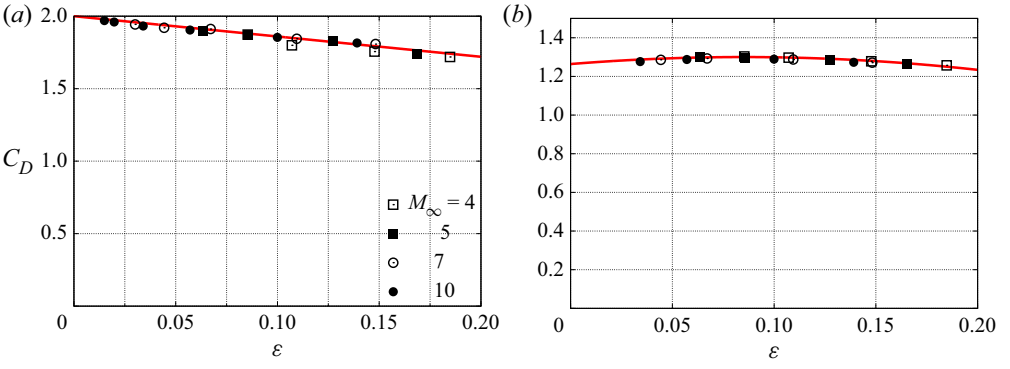

Figure 6. (*a*) Drag coefficient for flow over a 90° wedge with $M_\infty = 4$, 5, 7 and 10 and $\gamma = 1.05$, 1.1, 1.2 and 1.3. For $M_\infty = 10$, two cases of $\gamma = 1.01$ and 1.02, and with $M_\infty = 7$, one case with $\gamma = 1.01$ are added. (*b*) Drag coefficient for flow over a circular cylinder with $M_\infty = 4$, 5, 7 and 10 and $\gamma = 1.05$, 1.1, 1.2 and 1.3.

where the drag force is

$$D = 2L \int_0^H (p - p_\infty)\, \mathrm{d}y. \tag{2.4}$$

Here L is the transverse length of the wedge and y is the distance measured from the symmetry plane of the wedge. Then, if the form of (1.7) holds for C_D, expect that

$$C_D = g_1(\varepsilon) f_1(\eta_e). \tag{2.5}$$

The same set of computational results can now be used to check whether this is correct. Again we use the case of $\eta_e = 1$, where $f_1(1)$ is a constant, to check whether $g_1(\varepsilon)$ is unique. To this end, figure 6 shows a plot of C_D versus ε for the 90° wedge and for the circular cylinder. In both cases, all the results collapse onto a single line. For the 90° wedge,

$$C_D = g_1(\varepsilon) = 2 - 1.4\varepsilon, \tag{2.6}$$

and for the circular cylinder,

$$C_D = 1.3 - 5(\varepsilon - 0.085)^2. \tag{2.7}$$

In these two cases, the drag coefficients may be compared with the values from the Newtonian approximation, which are 2.0 and 4/3 for the 90° cone and the circular cylinder, respectively, both of which are fairly close to the curves of figure 6. To determine the form of the function $f_1(\eta_e)$, figure 7 shows four plots of $C_D/g_1(\varepsilon)$ versus η_e. Although the results agreed approximately with

$$f_1(\eta_e) = 0.85 + 0.15\eta_e, \tag{2.8}$$

they were scattered fairly broadly around the line, so that the validity of the functional form was not as convincing as in the case of the shock stand-off distance.

3. High-enthalpy effects

The present results were obtained from perfect-gas computations. However, it is possible that they apply also to flows at high enthalpy, where vibrational excitation and dissociation may occur and non-equilibrium effects become important. In the case of blunt bodies,

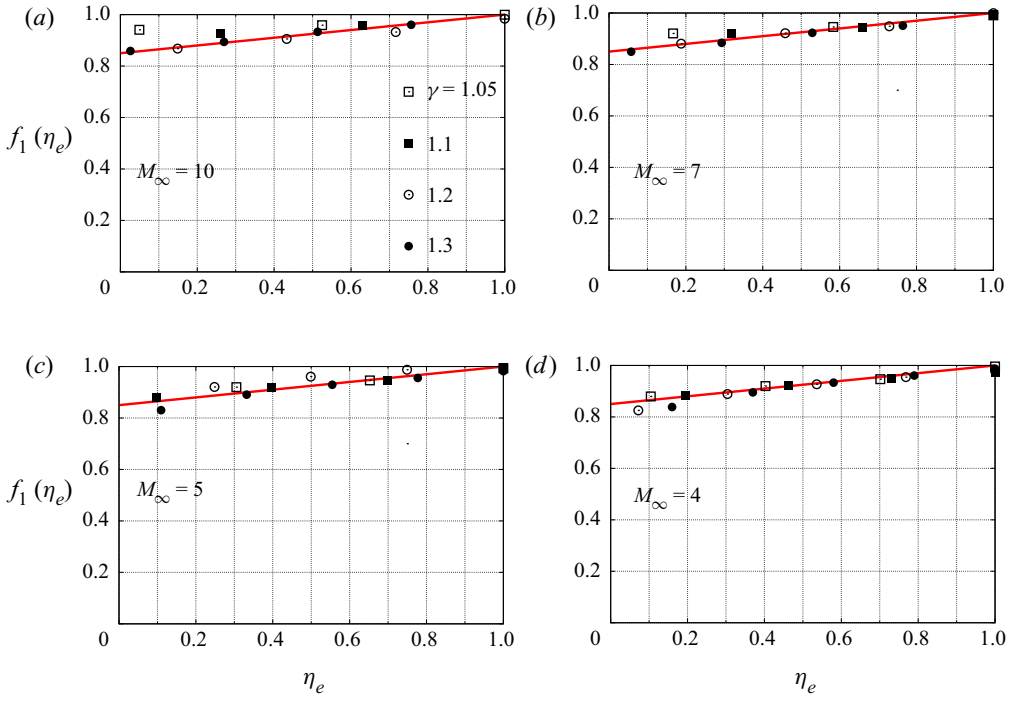

Figure 7. Four plots of $f_1(\eta_e)$ versus η_e: (*a*,*b*) $M_\infty = 10$ and 7; (*c*,*d*) $M_\infty = 5$ and 4. In all four plots, the line is the same and given by (2.6).

Wen & Hornung (1995) and Stulov (1969) showed that forming the density ratio with the average density along the stagnation streamline, instead of with the post-normal-shock density, causes such results to carry over to the high-enthalpy regime. This was shown by applying the conservation of mass to a control volume. Thus, in the case of blunt bodies, the manifold intricacies of high-enthalpy non-equilibrium flows influence the shock stand-off distance only through their substantial effect on the stagnation-line density profile. It would be interesting if this could be extended to the case of flow over a wedge, an idea requiring extensive work to be tested.

4. Conclusions

It was shown that the reduction from three independent parameters to two in the parameter space defining the dimensionless shock stand-off distance and drag coefficient, which was previously found for axisymmetric hypersonic flow over cones, applies also to flow over wedges in the detached-shock range. Useful analytical forms were found for these relations by performing a large number of Euler computations and plotting the results in an appropriate form. The results are also compared with new results for flow over a circular cylinder.

Funding. This work was funded by the US Air Force Office of Scientific Research, contract no. FA9550-19-1-0219, PI J.M. Austin, Contract Officer I.A. Leyva.

Declaration of interest. The author reports no conflict of interest.

Author ORCIDs.
H.G. Hornung https://orcid.org/0000-0002-4903-8419.

Appendix

The software system Amrita, constructed by James Quirk (see Quirk 1998), was used. A detailed description of the features and phenomena encountered with some of the algorithms used for Riemann solvers, including the one used here, has also been given by Quirk (1994). An example of a test of the software against experiment may be found in Quirk & Karni (1996).

Amrita is a system that automates and packages computational tasks in such a way that the packages can be combined (dynamically linked) according to instructions written in a high-level scripting language. The present application uses features of Amrita that include the automatic construction of the Euler solver, documentation of the code, adaptive mesh refinement according to simply chosen criteria, and scripting-language-driven computation, archiving and post-processing of the results. The automation of the assembly and sequencing of the tasks result in a dramatically reduced possibility of hidden errors. This technique also makes computational investigations transparent and testable by others. The ability to change one package at a time, without changing the rest of the scheme, facilitates the detection of sources of error. In most of the work, the Euler solver generated was an operator-split scheme with HLLE flux (after Harten, Lax & van Leer (1983) and Einfeldt (1988)) and kappa-MUSCL reconstruction. In some cases with γ close to 1, the carbuncle problem arose, and the more robust equilibrium flux method of Pullin (1980) was used. The (x, y) plane was discretized by a Cartesian grid of 300×300 coarse-grid cells that were adaptively refined by a factor of 3 to make an effective grid of 900×900 cells. The criterion for adaptation was a chosen threshold of the magnitude of the density gradient. Solid boundaries are represented by a level set defined as the smallest distance of a field point from the solid boundary. The grey shading of the visualizations is a monotonic function of the magnitude of the density gradient.

References

Chapman, C.J. 2000 *High Speed Flow*. Cambridge Texts in Applied Mathematics. Cambridge University Press.

Einfeldt, B. 1988 On Godunov-type methods for gas dynamics. *SIAM J. Numer. Anal.* **25**, 294–328.

Harten, A., Lax, P.D. & van Leer, B. 1983 On upstream differencing and Godunov-type schemes for hyperbolic conservation laws. *SIAM Rev.* **25**, 35–61.

Hayes, W.D. & Probstein, R.F. 1959 *Hypersonic Flow Theory*. Academic Press.

Hornung, H.G. 1972 Non-equilibrium flow of nitrogen over spheres and circular cylinders. *J. Fluid Mech.* **53**, 149–176.

Hornung, H.G., Schramm, J.M. & Hannemann, K. 2019 Hypersonic flow over spheriсcally blunted cone capsules for atmospheric entry. Part 1, the sharp cone and the sphere. *J. Fluid Mech.* **871**, 1097–1116.

Pullin, D.I. 1980 Direct simulation methods for compressible inviscid ideal-gas flows. *J. Comput. Phys.* **34**, 231–240.

Quirk, J.J. 1994 A contribution to the great Riemann solver debate. *Intl J. Numer. Meth. Fluids* **18**, 555–574.

Quirk, J.J. 1998 Amrita — a computational facility (for CFD modelling). In *VKI CFD Lecture Series*, vol. 29. von Kármán Institute.

Quirk, J.J. & Karni, S. 1996 On the dynamics of a shock bubble interaction. *J. Fluid Mech.* **318**, 129–163.

Stulov, V.P. 1969 Similarity law for supersonic flow past blunt bodies. *Izv. Akad. Nauk SSSR Mekh. Zhidk. Gaza* **4**, 142–146.

Wen, C.-Y. & Hornung, H.G. 1995 Non-equilibrium dissociating flow over spheres. *J. Fluid Mech.* **299**, 389–405.